Structural Origin of the Band Gap Anomaly of Quaternary Alloy $Cd_xZn_{1-x}S_ySe_{1-y}$ Nanowires, Nanobelts, and Nanosheets in the Visible Spectrum

S. Joon Kwon,*,† Hae-Min Jeong,†,‡ Kinam Jung,† Doo-Hyun Ko,†,§ Hyungduk Ko,† Il-Ki Han,† Gyu Tae Kim,‡ and Jae-Gwan Park*,†

†Nanophotonics Research Center, Future Convergence of Technology Research Division, Korea Institute of Science and Technology (KIST), Seoul 136-791, Korea, ‡School of Electrical Engineering, Korea University, Seoul 136-713, Korea, and §Department of Applied Chemistry, Kyung Hee University, Yongin Si 446-701, Korea

ABSTRACT Single-crystalline alloy II–VI semiconductor nanostructures have been used as functional materials to propel photonic and optoelectronic device performance in a broad range of the visible spectrum. Their functionality depends on the stable modulation of the direct band gap (E_g), which can be finely tuned by controlling the properties of alloy composition, crystallinity, and morphology. We report on the structural correlation of the optical band gap anomaly of quaternary alloy $Cd_xZn_{1-x}S_ySe_{1-y}$ single-crystalline nanostructures that exhibit different morphologies, such as nanowires (NWs), nanobelts (NBs), and nanosheets (NSs), and cover a wide range of the visible spectrum (E_g = 1.96–2.88 eV). Using pulsed laser deposition, the nanostructures evolve from NWs *via* NBs to NSs with decreasing growth temperature. The effects of the growth temperature are also reflected in the systematic variation of the composition. The alloy nanostructures firmly maintain single crystallinity of the hexagonal wurtzite and the nanoscale morphology, with no distortion of lattice parameters, satisfying the virtual crystal model. For the optical properties, however, we observed distinct structure-dependent band gap anomalies: the disappearance of bowing for NWs and maximum and slightly reduced bowing for NBs and NSs, respectively. We tried to uncover the underlying mechanism that bridges the structural properties and the optical anomaly using an empirical pseudopotential model calculation of electronic band structures. From the calculations, we found that the optical bowings in NBs and NSs were due to residual strain, by which they are also distinguishable from each other: large for NBs and small for NSs. To explain the origin of the residual strain, we suggest a semiempirical model that considers intrinsic atomic disorder, resulting from the bond length mismatch, combined with the strain relaxation factor as a function of the width-to-thickness ratio of the NBs or NSs. The model agreed well with the observed optical bowing of the alloy nanostructures in which a mechanism for the maximum bowing for NBs is explained. The present systematic study on the structural–optical properties correlation opens a new perspective to understand the morphology- and composition-dependent unique optical properties of II–VI alloy nanostructures as well as a comprehensive strategy to design a facile band gap modulation method of preparing photoconverting and photodetecting materials.

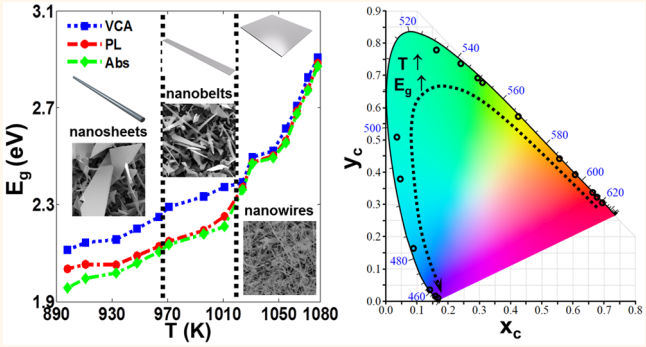

KEYWORDS: quaternary alloy · chalcogenide · II–VI chemical compound semiconductor · nanowires · nanobelts · nanosheets · band gap bowing · band gap modulation · empirical pseudopotential method · pulsed laser deposition

There are various methods for fabricating chemical compound semiconductor nanostructures in conjunction with band gap engineering[1–17] to meet the requirements of the applications in optoelectronic and photonic devices such as light-emitting diodes and lasers,[3,4,6,9,12,14,17] photocatalysts for oxidation and reduction of organic compounds,[2] photovoltaic devices,[1–5] and photoenhanced charge carrier platforms[5,11,15] used in the visible spectrum. These methods include conventional doping, which aims to control charge carrier mobility,[11] and the preparation of heteronanostructures to modulate electronic band structure,[14,15] employing quantum confinement effects[13] and alloying,[6–13,16,17] for example. In particular, alloying II–VI

* Address correspondence to cheme@kist.re.kr, jgpark@kist.re.kr.

Received for review March 9, 2015 and accepted April 21, 2015.

Published online April 21, 2015
10.1021/acsnano.5b01472

chemical compound (chalcogenide) single-crystalline semiconductors with nanoscale structures[8−10,12,13,16,17] provides facile ways of tuning optical and electronic transport properties and of enhancing photoconverting properties with reliable engineered modulation of band gaps over a broad range of the visible−IR spectrum. In contrast to the well-known quantum confinement effects, which are eminent when the structure of the semiconductors has feature size, such as radius (for quantum dots), length (for quantum rods), or thickness (for quantum wells), comparable to the Bohr radius (*i.e.*, ∼few nanometers), geometrical confinement effects concern semiconductor nanostructures of several tens of nanometers or larger size (*i.e.*, nanowires (NWs), nanorods, nanosheets (NSs), and nanoribbons). In particular, they are distinguishable from the quantum confinement effects in that they give rise to changes in intrinsic optical properties of the semiconductors due to strain development and relaxation,[8−12,14−17] sustaining crystallinity. This is due mainly to lattice mismatch among the different components in a limited dimension, which does not exceed the feature size of the structure by three or more orders of magnitude.[11,16−21]

As we had reported in a former study on the experimental and theoretical analysis of the structural and optical properties of binary alloy CdS_xSe_{1-x} NWs,[8] the geometrical confinement accompanied by formation of a thin and elongated single-crystalline structure requires the alloy NWs to relax residual strain in both the radial and the axial directions.[8,20] This strain relaxation results in optical property anomalies, such as the disappearance of the optical bowing, followed by linear dependence of the band gap as a function of the composition x.[8] The growth of the CdS_xSe_{1-x} NWs indicated that the strain relaxation is a prerequisite to sustain single crystallinity and maintain structural stability. In particular, the observed alloy NWs were stable, growing up to several tens of micrometers, because the lattice mismatch between hexagonal wurtzite (HWZ) crystalline CdS (c lattice constant = 6.683 Å) and CdSe (c lattice constant = 6.950 Å) is relatively small (*i.e.*, 3.835%).[22,23] Being without optical bowing effects, the alloy NWs were found to be relevant for band gap modulation between 1.75 and 2.45 eV in a linear manner.[8]

For quaternary alloy nanostructures composed of ZnS, ZnSe, CdS, and CdSe, it is expected that the facile band gap modulation and wide coverage are more promising than with simple binary alloy nanostructures. Recently, Pan *et al.* reported a series of experimental studies on the band gap modulation of the quaternary alloy NWs and NBs, which cover nearly the entire range of the visible spectrum.[16,17] There are, however, still several potential barriers concerning the preparation and utilization of the quaternary alloy nanostructures for the facile band gap engineering. First, to obtain enhanced optical properties, it is required to prepare the alloy nanostructures in a single-crystalline solid solution with the same crystalline symmetry. In the case of the quaternary nanostructures, the lattice mismatch is relatively large (*i.e.*, from c lattice constant of 5.430 Å of HWZ ZnS to 6.950 Å of HWZ CdSe with the maximum lattice mismatch up to 21.867%), and the equilibrium crystal structures would be different at room temperature (*i.e.*, cubic zinc blende for ZnS, ZnSe, and CdS *vs* HWZ for ZnS, CdS, and CdSe).[22,23] Additionally, there is a non-negligible bond length mismatch between ZnS (2.335 Å) and CdSe (2.630 Å), mainly due to a large difference in cation size between Zn^{2+} (0.880 Å) and Cd^{2+} (1.090 Å).[22,23] These structural and bond length mismatch factors can result in an unrelaxed strain, which gives rise to unexpected intrinsic atomic disorder[24−26] in the nanostructures. Last, it should also be noted that there is a considerable gap in melting points of the II−VI components (*i.e.*, from 1458 K for ZnS to 2023 K for CdS), and therefore, a non-negligible difference in the degree of the supersaturation of each component in the vapor phase is developed,[22,23] which can lead to different condensation kinetics of vapor-phase precursors. In turn, the different condensation kinetics can result in microphase separation (*i.e.*, local dealloying, formation of microdomains or polycrystalline structures) and prevent the solid solution from forming at equilibrium. These factors could work together in limiting design of the arbitrary composition for the stable form of quaternary alloy nanostructures, especially for the nanostructures intervened with the well-known vapor−liquid−solid (VLS) mechanism. In addition, they affect the morphological evolution of the alloy nanostructures, not only the NWs but other forms such as NSs and nanobelts (NBs). Thus, it is important to analyze and understand the complex correlations among the composition, structural stability, morphology, crystallinity, and optical properties of the quaternary alloy nanostructures prior to designing the band gap modulation strategy.

In the present study, we report a structure−optical anomaly correlation in the quaternary alloy $Cd_xZn_{1-x}S_ySe_{1-y}$ nanostructures that involves NWs, NBs, and NSs in the nearly full visible spectrum. A vapor-phase transport method was used to synthesize quaternary alloy $Cd_xZn_{1-x}S_ySe_{1-y}$ nanostructures in which the spatial gradient of the growth temperature is used to control the composition. In contrast to the chemical vapor deposition method incorporated with a double gradient method (DGM-CVD), which uses two spatially separated powder sources to prepare the quaternary alloy NWs and NBs suggested by Pan *et al.*,[16,17] we employed a single sintered source under a continuous laser pulse to obtain an ablated plume of the four components simultaneously, which is transported to the substrate at which the growth temperature is

controlled to condense and let the precursor plume be crystallized with different compositions in various morphologies of the nanostructures.[8] Given different compositions (x and y) at different growth temperatures, we observed three different morphologies of the single-crystalline HWZ nanostructures such as NWs, NBs, and NSs, which covered a broad range of band gaps of 1.96−2.88 eV corresponding to the nearly full visible spectrum. These different nanostructures showed different optical properties, such as the disappearance of optical bowing for NWs[8] and maximum optical bowing for NBs and slightly smaller bowing for NSs. We used a computational method based on an empirical pseudopotential method (EPM) to determine the structural origin underlying the observed structure-dependent band gap anomaly,[27−35] and it turned out that there residual strain existed for NBs and NSs up to −1.4 (compressive strain) to 1.5% (tensile strain). By analyzing volumetric strain and the bond length mismatch factor as a function of the composition, we found that the intrinsic atomic disorder decreased as the morphology of the nanostructures evolved from NWs *via* NBs to NSs, which implies the existence of a morphology-dependent strain relaxation factor to reconcile the observed optical bowing anomaly. We found a semiempirical equation determining the structure−band gap anomaly correlation as a function of morphological parameter such as the width-to-thickness ratio of the nanoplate-shaped structures, which agrees well with the experimental observation. The present study is expected to provide a comprehensive understanding of the underlying structural−optical properties correlation of II−VI alloy nanostructures of a variety of morphologies. With a deeper understanding, a more accurate, reliable, and facile band gap modulation strategy targeting the visible spectrum can be constructed, and the strategy can be employed to enhance light-emitting, photovoltaic, photocatalytic, and photosensitive performances, targeting applications in a broad range of the visible spectrum.

RESULTS

Growth of the Quaternary Alloy $Cd_xZn_{1-x}S_ySe_{1-y}$ Nanostructures. Shown in Figure 1a are scanning electron microscopy (SEM) images of alloy $Cd_xZn_{1-x}S_ySe_{1-y}$ nanostructures with different compositions monotonically varying from [x, y] = [0.980, 0.201] (at 898 K) to [0.308, 0.342] (at 1078 K) grown at different temperatures. The growth temperature range was varied with changing distance, d, from the target under laser ablation to the substrate on which the alloy nanostructures grow. We observed that the temperature can be controlled continuously from 1100 to 880 K with increasing d (refer to Figure S1 in the Supporting Information (SI) for the relationship between the growth temperature (T) and d). As presented in the figures, the different growth temperatures give rise to different geometries from NWs at higher growth temperature (1024−1078 K) intervened by NBs in the intermediate temperature range (971−1011 K) to NSs at lower temperatures (898−945 K). From this observation, it can be considered that the nanostructures suffer from morphological evolution from NWs *via* NBs to NSs, in order, with increasing the degree of supersaturation resulting from decreasing growth temperature. The NWs have diameters ranging from 85 to 105 nm and lengths of 25−40 μm, while the width of the NBs was up to 0.85−1.45 μm and a thickness and length of 95−110 nm and ∼12 μm, respectively. For the NSs, the thickness ranges from 90 to 110 nm, and the area of the sheets was up to 480−930 μm^2. The X-ray diffraction (XRD) data for the alloy nanostructures indicate that the nanostructures form solid solution phases regardless of the composition and morphology of the structure. Notably, the alloy nanostructures maintain the same crystallinity of HWZ throughout the morphological evolution, as presented in Figure 1b, in which the 2θ positions of the peaks corresponding to [002] and [100] directions are commonly shifted from 24.14 and 25.62° at 898 K to 25.52 and 26.60° at 1078 K, with the increasing growth temperature. This means that the alloy nanostructures are solid solutions in a single-crystalline form.

To check the growth mechanism of the alloy nanostructures, we further explored the morphological evolution, as shown in the SEM images in Figure 1c−e. In the magnified insets, we can observe a clear interface between a small Au alloy tip and the end or the edge of the nanostructures (*i.e.*, NWs in (c), NBs in (d), and NSs in (e)). A clearer dark-field TEM (transmission electron microscopy) image for the Au−NW interface is given in Figure S2 in the SI. From these observations, the growth of the alloy nanostructures is believed to be governed by the well-known VLS phase transition mechanism regardless of the composition and morphology. According to the thermodynamic model for the VLS process,[36] it is believed that the supersaturated liquid-phase materials diffuse out of the Au alloy nucleus followed by growth (*i.e.*, phase transition), resulting in the formation of the elongated solid-phase geometry such as NWs. For certain conditions, the grown NWs would suffer further morphological instability accompanied by transition: NWs to NBs *via* side branching, which would result from the surface instability of the NWs accompanied by concentration undulation along the NWs' elongated direction.[37] With the continuous branch-filling process, NBs can be developed into wider morphologies such as NSs. The detailed mechanism for the morphological evolution of the alloy nanostructures with a theoretical model and computational approach, such as the phase field model for the phase transition, is out of the present study's focus, although helpful information can be found in the literature.[36−39]

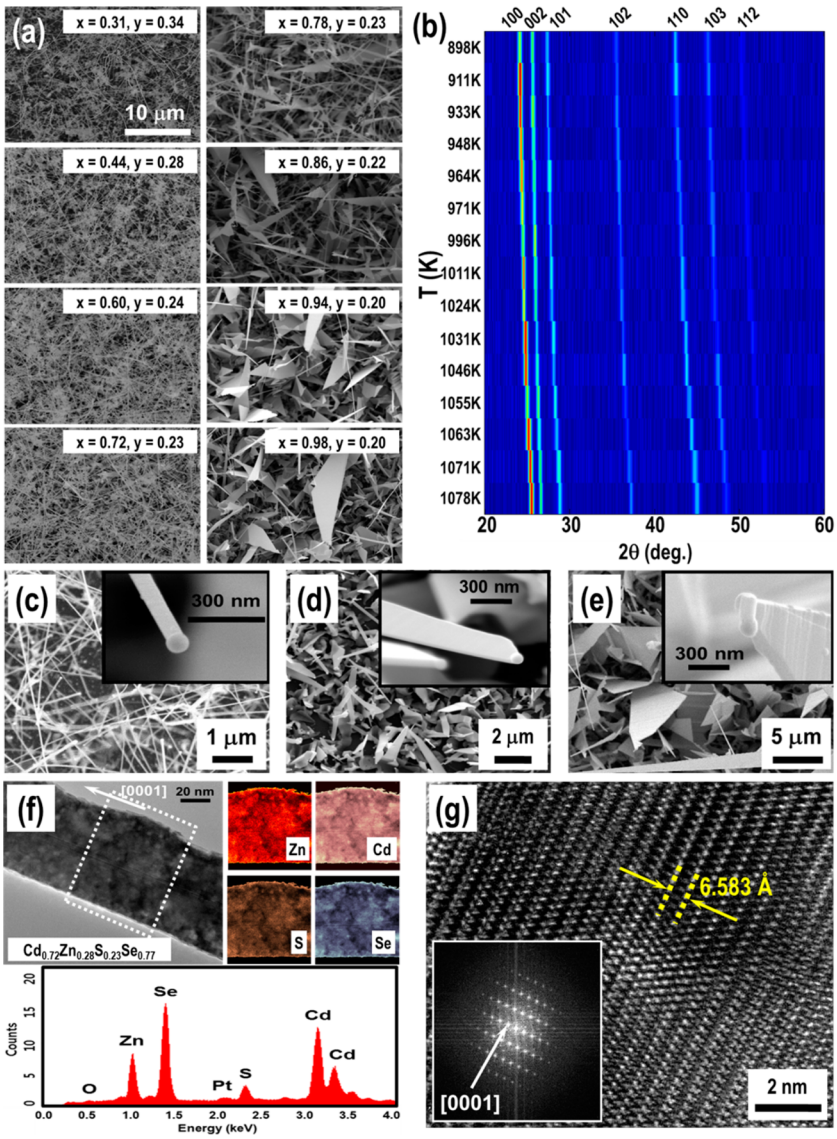

Figure 1. (a) SEM images of quaternary alloy $Cd_xZn_{1-x}S_ySe_{1-y}$ nanostructures grown at different temperatures (T = 1078–898 K from top left to bottom right in order) with different compositions (x and y). (b) Color-mapped XRD data for the alloy nanostructures grown at different T with crystalline indices matched for the HWZ crystal structure. (c–e) Representative SEM images for the different morphologies of the alloy nanostructures (*i.e.*, NWs, NBs, and NSs in (c), (d), and (e), respectively) with insets for the magnified SEM images of the edge of the structures that is attached to Au alloy tips. (f) Bright-field TEM image of the alloy NWs (x = 0.72 and y = 0.23) accompanied by spatial mapping of the elemental distributions of Zn, Cd, S, and Se (colored images) and EDS for each of the elements in the NWs. (g) HR-TEM image for the alloy NWs with the inset of the selected area electron diffraction pattern showing the crystallinity identified as HWZ. In the HR-TEM image, the c lattice parameter is depicted with yellow dotted lines.

We further tried to check the formation of a solid solution phase of the alloy nanostructures by examining elemental distributions of Cd, Zn, S, and Se over the structures using energy-dispersive X-ray spectra (EDS) accompanied by TEM. One of the representative analysis results is given in Figure 1f for $Cd_{0.72}Zn_{0.28}S_{0.23}Se_{0.77}$ NWs, in which we can confirm that there is no spatial or elemental correlation in the elemental distribution data obtained from EDS mapping (top panel of Figure 1f). This indicates that the spatial distributions of the four different elements in the structure are nearly uniform, excluding the possibility of the microphase separation or dealloying. We also found similar results for other alloy nanostructures. This also confirms the formation of the solid solution of the four components (CdS, CdSe, ZnS, and ZnSe) in the single-crystalline alloy nanostructures. From the EDS data (bottom panel of Figure 1f), we can also calculate the atomistic fraction of each of the components in the alloy nanostructures, which can be translated into the compositions x and y. Finally, we used HR-TEM to observe the single crystallinity and measure lattice parameters of the alloy nanostructures directly. One of the representative results is given in Figure 1g for $Cd_{0.72}Zn_{0.28}S_{0.23}Se_{0.77}$ NWs. As shown in the HR-TEM image accompanied by a selected area electron

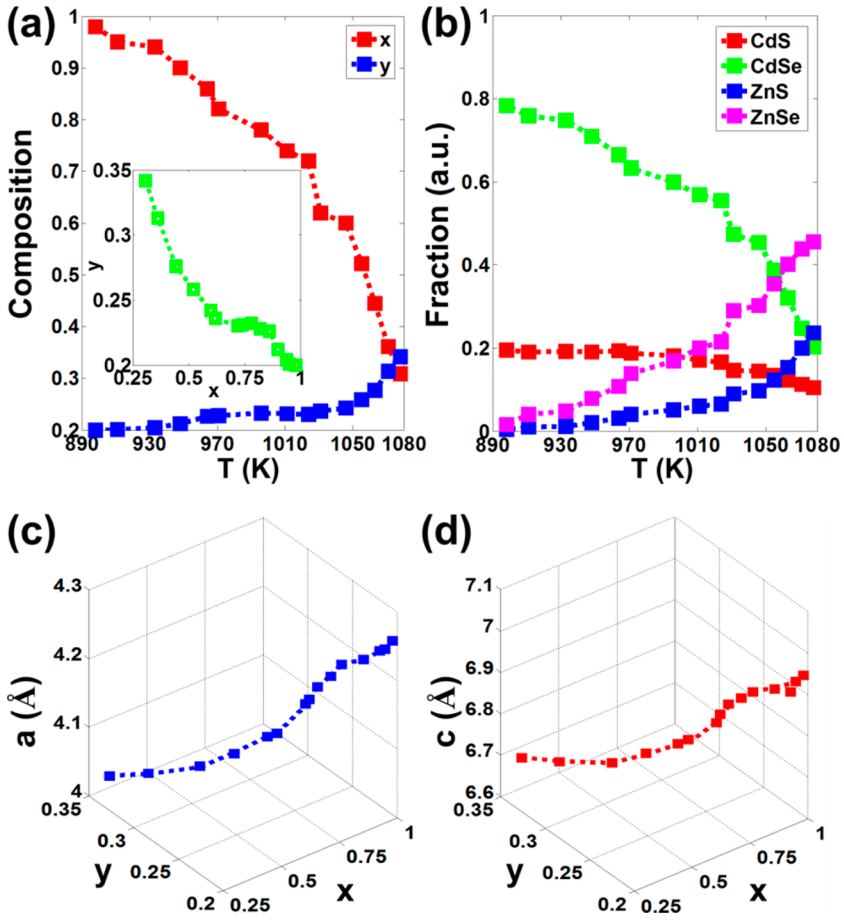

Figure 2. (a) Variations of the compositions *x* and *y* in the alloy nanostructures as a function of *T*. Inset is the relationship between *x* and *y*. (b) Variations of the molar fractions of CdS, CdSe, ZnS, and ZnSe in the alloy nanostructures as a function of *T*. (c) Systematic change of the experimentally measured lattice parameter *a* of the HWZ single-crystalline alloy nanostructures as a function of the compositions *x* and *y* (squares) with expected values obtained from the virtual crystal approximation model (dotted line). (d) Same as (c) except for the lattice parameter *c*.

diffraction pattern, we can confirm that the alloy nanostructures have single crystallinity of HWZ. In particular, the NWs were observed to grow preferentially along the [0001] direction, which is parallel to the *c*-axis of the HWZ crystal structure.

From the EDS, HR-TEM, and XRD analysis with a Bragg relationship, we analyzed the dependences of the component fraction and the composition of the alloy nanostructures as a function of growth temperature. To calculate the composition of the alloy nanostructure, we employed a linear approximation relationship such that

$$Cd_xZn_{1-x}S_ySe_{1-y} = [CdS]_{xy} + [CdSe]_{x(1-y)} + [ZnS]_{(1-x)y} + [ZnSe]_{(1-x)(1-y)} \quad (1)$$

As shown in Figure 2a,b, the value of *x* decreases and the value of *y* increases with increasing growth temperature. As a result, the component fractions of CdS and CdSe decrease with increasing growth temperature, whereas the component fractions of ZnS and ZnSe increase. This behavior is not surprising because the eutectic points of the ZnS−Au and ZnSe−Au are higher than those of the CdS−Au and CdSe−Au. Due to differences in the melting point and eutectic point, molar fractions of each of the components in the vapor phase before suffering from the vapor−solid transition are different, which results in the difference in the degree of supersaturation and differences in the component fraction. Notably, it is observed that *x* and *y* have an inverse proportional relationship (inset of Figure 2a), although it is not a mathematically simple inverse proportional relationship. This correlation would indicate that the growth process involves vapor-phase transport of CdS, CdSe, ZnS, and ZnSe molecular precursors, not of ionic precursors Cd^{2+}, Zn^{2+}, S^{2-}, and Se^{2-}.[18,19,21] In particular, if the process involves the ionic precursors, there would be no correlation between *x* and *y*. It should also be noted that the component fraction ratio between ZnSe and ZnS is nearly constant with increasing growth temperature, whereas the ratio between CdSe and CdS decreases continuously. This is due mainly to the fact that the composition of sulfur is relatively lower than other compositions throughout the growth process. Interestingly, this tendency is consistent with the experimental observation of solid solution stability of

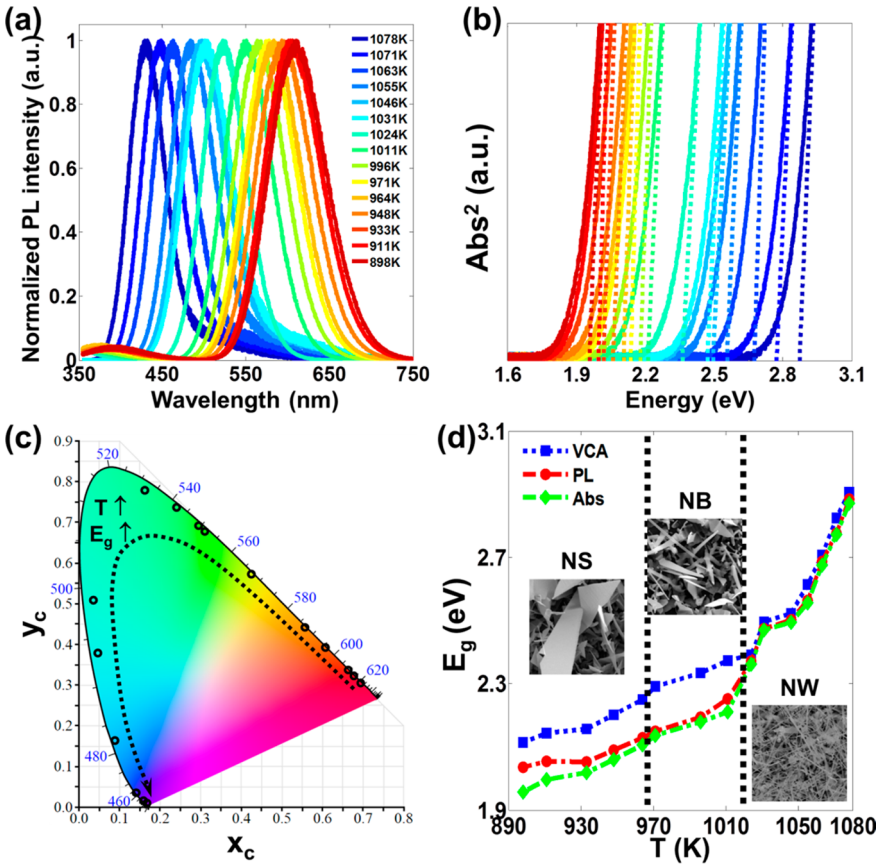

Figure 3. (a) Normalized PL and (b) squared UV−vis Abs spectra of the alloy nanostructures grown at different *T*. For Abs, asymptotes (dot lines) are given for the squared intensity of the spectra to indicate the *x*-axis intercepts that correspond to the lowest direct band gaps (E_g) of the alloy nanostructures. (c) Visible colors translated from the PL spectra fixed on the CIE-1931 color map. In the color map, x_c and y_c are the color coordinates defining color in the map. (d) Dependence of E_g as a function of *T*: expected values from the VCA model (blue symbols and dotted line) and experimentally measured values obtained from the PL (red symbols and dash-dotted line) and Abs (green symbols and dash-dotted line) spectra. Vertical black dashed lines are given to indicate different morphologies, such as NWs, NBs, and NSs that exhibit an optical bowing anomaly.

alloy $Cd_xZn_{1-x}S_ySe_{1-y}$ quantum wells; CdZnSSe is more stable than CdZnSe with a high vapor pressure of Zn.[21] Combining the composition and the component fraction analysis with XRD and HR-TEM analysis, we analyzed the dependence of the HWZ lattice parameters *a* and *c* as a function of the growth temperature. As shown in Figure 2c,d, the lattice parameters are effectively described by Vegard's law such that

$$I = I_{CdS}xy + I_{CdSe}x(1-y) + I_{ZnS}(1-x)y + I_{ZnSe}(1-x)(1-y), I = a \text{ and } c \quad (2)$$

Consistent with Vegard's law, the solid solution alloy nanostructures satisfy a model determined by the virtual crystal approximation (VCA).[40] This also implies that the geometric properties of the as-grown alloy nanostructures having the same point group constituents are determined by the ensemble average over the geometric properties of the component materials, as is usually the case in the context of laser-deposited pseudobinary alloy CdSSe thin films[41] and quaternary alloy CdZnSSe thin films.[42]

Optical Properties and Band Gap Bowing of the $Cd_xZn_{1-x}S_ySe_{1-y}$ Nanostructures. We further explored optical properties of the alloy nanostructures by using photoluminescence (PL) and UV−visible absorbance (Abs) spectra. It is well-known that the II−VI single-crystalline semiconductor alloys composed of CdS, CdSe, ZnS, and ZnSe have a direct band gap,[22,23,26,29,30,43] and therefore, PL and Abs analysis is one of the most quantitative methods to measure the direct band gap, E_g, of the alloy nanostructures. As shown in Figure 3a, a clear red shift in PL can be observed when the fractions of the CdS and CdSe are relatively abundant with decreasing growth temperature. This shift also confirms that the direct E_g can be easily modulated in the visible spectrum by controlling the growth temperature as Pan *et al.* reported in recent experiments on quaternary alloy $Cd_xZn_{1-x}S_ySe_{1-y}$ NWs and NBs.[16,17] From the PL analysis, the capability of band gap modulation was observed to cover nearly the full range of the visible spectrum, such as 2.04 (λ = 608.8 nm) to 2.88 eV (λ = 429.6 nm).

To find out whether the band gap modulation of the alloy nanostructures originates from the intrinsic electronic properties of the alloy structures or morphology-dependent factors, we also analyzed the Abs spectra (Figure 3b). As is apparent from the figure, the

x-intercept of the extrapolation asymptotes for the squared Abs intensity also shows a clear red shift in E_g with decreasing growth temperature. Notably, the observed values of E_g obtained from the Abs intensity are slightly smaller than those from the PL spectra, although a similar capability of covering nearly the full range of the visible spectrum is acquired again (*i.e.*, 1.96 eV (λ = 633.1 nm) to 2.87 eV (λ = 431.4 nm)). To check the applicability of the alloy nanostructures for photonic devices such as photodetectors or multicolor laser materials, we matched the observed PL spectra with the visible color obtained from the CIE-1931 color map (refer to Figure 3c). As pinned in the map, continuously varying color coordinates of the alloy nanostructures clearly indicate that the alloy nanostructures can cover nearly the full visible spectrum. Thus, the alloy nanostructures synthesized are suitable as functional materials for photovoltaic, photocatalytic, multispectral light-emitting, and photosensitive devices with applicability in the visible spectrum.

Finally, we tried to compare the expected value of E_g of the alloy nanostructure calculated from the VCA model with the experimentally measured values. For the VCA model, the change in E_g ($E_{g,VCA}(x,y)$) can be described simply as a concentration-weighted linear combination of E_g of pure components such that

$$E_{g,VCA}(x,y) = E_{g,CdS}xy + E_{g,CdSe}x(1-y) + E_{g,ZnS}(1-x)y + E_{g,ZnSe}(1-x)(1-y) \quad (3)$$

where the model generally assumes the single crystallinity with no deformation of the unit cell and a negligible amount of inner defects or residual strain at equilibrium.

As is apparent from Figure 3d, $E_{g,VCA}$ is larger than the experimentally observed values of E_g regardless of the measurement method. This difference in E_g is the optical bowing in the alloy semiconductor,[24,25,30,31,33−35,41−43] which can be translated into following equation

$$E_g(x,y) = E_{g,VCA}(x,y) - B_1x^2(B_2+y) - B_3y^2(B_4+x) \quad (4)$$

where the optical bowing effect can be mathematically described by a third or higher degree polynomial.[30] In eq 4, we assumed that the optical bowing effect is mostly described by a third degree polynomial with the bowing parameters B_1, B_2, B_3, and B_4.[30] From the PL and Abs analysis, we observed that the bowing effect is 0.12−0.15 eV, depending on the growth temperature (and, therefore, on composition and morphology). Interestingly, this value is considerably smaller than the expected maximum bowing for the ternary alloy (*i.e.*, <0.6 eV (=2.4 × 0.5^2 eV)).[44]

For alloy semiconductors, Van Vechten and Bergstresser proposed that the bowing effect is ascribed by intrinsic bowing due to disorder in the virtually ordered crystal and the extrinsic bowing due to short-range atomic aperiodicity.[24,25] We can exclude the extrinsic bowing factor because the observed nanostructures have considerably long or wide dimensions in which defects given by the short-range atomic aperiodicity are negligible. For the intrinsic bowing, there are several factors that determine the magnitude of the bowing such as the local fluctuation of the core atomic potentials, through the analysis of the coherent potential approximation calculations,[44] the linear electronic density functional approximation,[45] and pseudopotential methods in the special quasi-random structure.[46] The intrinsic bowing parameter is also found to be strongly dependent on the thermodynamic relationship of the inner disorder of the virtually ordered alloy.[47] For the intrinsic factors in the case of a pseudobinary cubic crystalline semiconductor alloy ($A_xB_{1-x}C$), Zunger and Jaffe pointed out the bond length disorder confined in the unit cell, which gives rise to the atomic displacement of anions (C) from the designated position can result in the notable bowing.[25] For the HWZ quaternary alloy semiconductor, the displacement of cations and bond length mismatch are expected to be greater than those in the binary alloy, and therefore, it is not surprising to observe optical bowing in the present study. Notably, however, the difference between $E_{g,VCA}$ and the observed E_g was negligible for the alloy NWs. This indicates that the optical bowing disappears even when the compositional entropy is not negligible. In particular, the compositional entropy per unit volume ΔS can be written as

$$\Delta S = -k_B[x\ln x + (1-x)\ln(1-x) + y\ln y + (1-y)\ln(1-y)] \quad (5)$$

where k_B is the Boltzmann constant. For ΔS, we assumed no deformation of the unit cell. Indeed, ΔS is comparable to the theoretically expected maximum value of ΔS (*i.e.*, $\Delta S = 1.276k_B$ when $x = 0.444$ and $y = 0.276$, which is close to the maximum value such that $\Delta S|_{max} = 1.386k_B$ when $x = y = 0.50$). This is a notable finding considering that the bowing effect usually approaches the maximum when ΔS is getting closer to $\Delta S|_{max}$ accordingly.[8] More importantly, in contrast, the difference in E_g is distinctive for the alloy NBs and NSs. Additionally, the bowing effect is more prominent for the alloy NBs compared to NSs. This observation appears to not be consistent with the experimental observations of optical properties of $Cd_xZn_{1-x}S_ySe_{1-y}$ NWs and NBs reported by Pan *et al.*,[16,17] where they observed almost no optical bowing for all NWs and NBs of arbitrary composition.

By examining the morphological characteristics from image analysis and the bowing properties, it is appropriate and possible to differentiate the NWs and NBs. Admittedly, it can be difficult to distinguish NBs and NSs by just examining apparent morphology or by measuring bowing properties. To secure a solid

distinction, we will explore further structural and optical property correlations from which more quantitative and fundamental standards for differentiating NBs from NSs are provided. From the perspective of a simple VCA model, the disappearance of the band gap bowing for the alloy NWs indicates that the residual strain would be negligible. In contrast, the bowing in the alloy NBs and NSs indicates that there is residual strain. From these observations, we can suggest that the optical bowing effect due to residual strain depends on the morphology and intrinsic atomic disorder in the unit cell.

DISCUSSION

Analysis of Residual Strain in the $Cd_xZn_{1-x}S_ySe_{1-y}$ Nanostructures. To examine how the different morphologies and atomic disorders would affect the residual strain and the optical bowing effect in the alloy nanostructures, we tried to find a correlation between the optical bowing factor and the structural properties of the alloy nanostructures. It is known that the band gap of a semiconductor can be reduced by residual strain, which produces deformation potential.[33−35] Thus, we explored the influence of residual strain on band gap variation. For the quantitative analysis, we used a simple computational method based on the EPM to calculate the electronic band structure with different compositions. Ever since it was conceived by Fermi,[48] EPM has been shown to be effective and accurate for calculating electronic structures of metals and semiconductors given fitting parameters that describe the experimental observations.[27−35,44] In the EPM, the atomic factors and pseudopotential parameters are adjusted to fit with the known experimental data, and therefore, it is one of the most efficient and effective methods to calculate the electronic band structures of alloy semiconductors in conjunction with VCA. We used the EPM with known atomic factors and pseudopotential parameters for the quaternary alloy nanostructures with different compositions.[27−30] Although there are specific computational approximation models dealing with the NS geometry in conjunction with the EPM, such as the super cell method,[33,34] we used a periodic boundary condition (unconfined Bloch model) for the calculation. This is mainly due to the fact that the observed structures of NBs and NSs are much bigger than the usual dimensions for which the super cell method can be applied. Usually, the super cell method can calculate the electronic band structure of the NSs composed of several thousand atoms, which, in turn, has dimensions of at most a 10 × 10 nm^2 monolayer sheet. This dimension is much smaller than that of the observed NBs or NSs. For the study on the effects of strain built inside the structures, we also introduced biaxial strain (parallel to the NBs or NS plane) to the alloy NBs or NSs under the EPM calculation. Detailed procedures and information on the computational method based on the EPM are given in the SI.

Shown in Figure 4a,b are the calculated electronic band structures of the single HWZ crystalline alloy NBs (*i.e.*, $Cd_{0.78}Zn_{0.22}S_{0.23}Se_{0.77}$ NBs in (a)) and NSs (*i.e.*, $Cd_{0.95}Zn_{0.05}S_{0.20}Se_{0.80}$ NSs in (b)) with different residual strains. In the calculated band structures, we can confirm the existence of the direct band gap between conduction (Γ_c) and valence band (Γ_v) at the Γ symmetry point of the Brillouin zone regardless of the morphology, composition, or residual strain. For the strained NBs and NSs, both the compressive ($\Delta\varepsilon < 0$) and the tensile ($\Delta\varepsilon > 0$) strain affect the reduction in the band gap.[33−35] By comparing the calculated data for NBs and NSs, it was also found that the higher the residual strain, the greater the band gap reduction and, therefore, the greater the positive band gap bowing.

Using EPM, we found the responsible residual strain in the alloy NBs or NSs in the tensile or compressive direction. In Figure 4c, the calculation result is summarized as a function of the growth temperature. As is apparent from the figure, there is a continuous but abrupt change in the residual strain in the alloy nanostructures at a certain growth temperature between 964 and 971 K. This certain point would imply the existence of a transition point between the NBs (*i.e.*, narrow nanoplates) and NSs (*i.e.*, wide nanoplates). Indeed, this is supported by the observation of the morphological evolution of the nanoplate-shaped structures. For example, for a growth temperature above 971 K, the ratio between the width (L) and thickness (D) of the nanoplates is L/D = 4.8−9.8, whereas it increases to L/D = 19.3−92.6 by 1 order of magnitude when the growth temperature is below 964 K. Thus, there is a morphological evolution point that is similar to the phase transition point, although there is no physical change in the crystallinity of the alloy nanostructures. Based on this observation, we sorted the alloy nanoplates into NBs or NSs. Another notable point in Figure 4c is that the residual strain in each structure is relatively constant. For example, the average calculated residual strain built in the alloy NBs is 1.280 ± 0.157% (for tensile strain) or −1.273 ± 0.150% (for compressive strain). For the alloy NSs, the average residual strain is calculated as 0.564 ± 0.115% (for tensile strain) or −0.546 ± 0.123% (for compressive strain). These calculated results indicate that the development of the residual strain in the alloy nanostructures is determined mainly by morphology of the alloy structures. In order to check this proposition, we tried to find a fitting parameter set for the optical bowing in eq 4 for NBs and NSs. The bowing parameters are mainly determined by intrinsic structural properties such as atomic disorder and residual strain, and therefore, we can suppose that there exists a unique set of bowing parameters that determine the optical bowing given a specific residual strain.[24,25,44−47] With

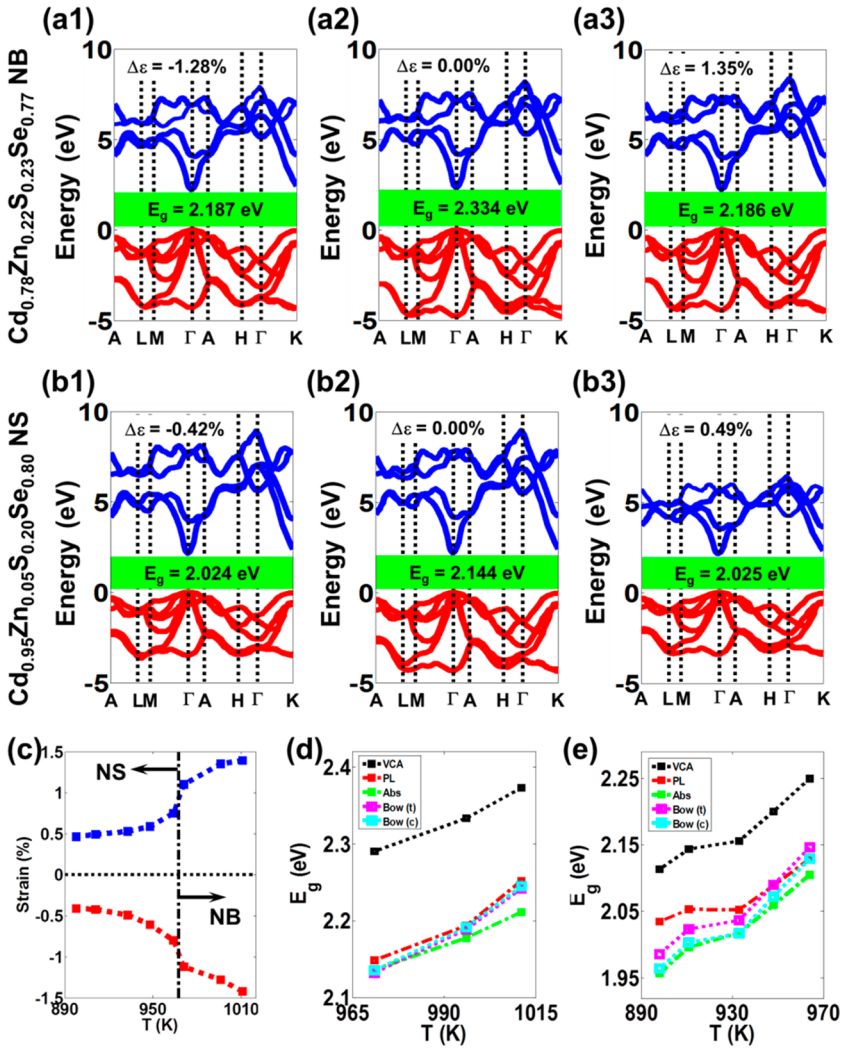

Figure 4. Calculated electronic band structure diagrams of the quaternary alloy nanobelts of $Cd_{0.78}Zn_{0.22}S_{0.23}Se_{0.77}$ with different residual strains ($\Delta\varepsilon$) (alloy NB in (a1−a3), in the first row) and nanosheets of $Cd_{0.95}Zn_{0.05}S_{0.20}Se_{0.80}$ with different residual strains (alloy NS in (b1−b3), in the second row). E_g in each electronic band diagram is depicted as a green rectangle located between the conduction band (Γ_c) and the valence band (Γ_v) fixed at the Γ symmetry point of the Brillouin zone of the HWZ unit cell. (c) Dependence of the calculated residual strain in the alloy NBs and NSs grown at different T calculated using the EPM. Blue and red symbols and lines are for the tensile and compressive strains, respectively. (d) Dependence of E_g with increasing T for the alloy NBs. Calculated values of E_g from the VCA model (black dotted lines) are compared with the experimentally observed values (PL (red) and Abs (green) dash-dotted lines) and calculated values obtained by the bowing equations with different bowing parameter sets which correspond to the alloy NBs with tensile (t, pink lines) and compressive (c, cyan lines) residual strains, respectively. (e) Same as (d) except for the alloy NSs.

a least-squares fitting method, we obtained fitting parameter sets for the alloy NBs such that [B_1, B_2, B_3, B_4] = [0.21, 0.10, 0.09, 0.08] (in eV for tensile strain) and [0.15, 0.31, 0.06, 0.12] (in eV for compressive strain) and for the alloy NSs such that [B_1, B_2, B_3, B_4] = [0.11, 0.08, 0.15, 0.02] (in eV for tensile strain) and [0.13, 0.09, 0.12, 0.05] (in eV for compressive strain), respectively. As shown in Figure 4d,e, the optical bowing relationship with the fitting parameters agrees with the experimental observations for both alloy NBs and NSs. With these findings, we can suggest that the alloy NBs and NSs are structurally distinguishable as well as optically different.

Next, we further investigated the structural origin that governs the observed anomaly of the optical properties of the alloy nanostructures. First, we sought to find a dependence of the volumetric strain ($\Delta\varepsilon_V$) by comparing the ratios between the linear combination of the concentration (f)-weighted unit cell volume of each component

$$V_S = \sum_i f_i v_i, v_i = 3^{1/2} a_i^2 c_i/2,$$
$$i = \text{CdS, CdSe, ZnS, and ZnSe} \quad (6)$$

and the virtual crystal unit cell volume $V_{VCA} = 3^{1/2}$-$a_{VCA}^2 c_{VCA}/2$ (where the subscript VCA denotes the VCA model) such that $V_S/V_{VCA} = 1 + \Delta\varepsilon_V$. It is also possible to calculate the biaxial strain factor $\Delta\varepsilon_{||}$ from $\Delta\varepsilon_V$ by the relationship $\Delta\varepsilon_V = (1 + \Delta\varepsilon_{||})^2(1 - \sigma\Delta\varepsilon_{||})$, where σ denotes Poisson's ratio. Here, $\Delta\varepsilon_{||}$ is not physically

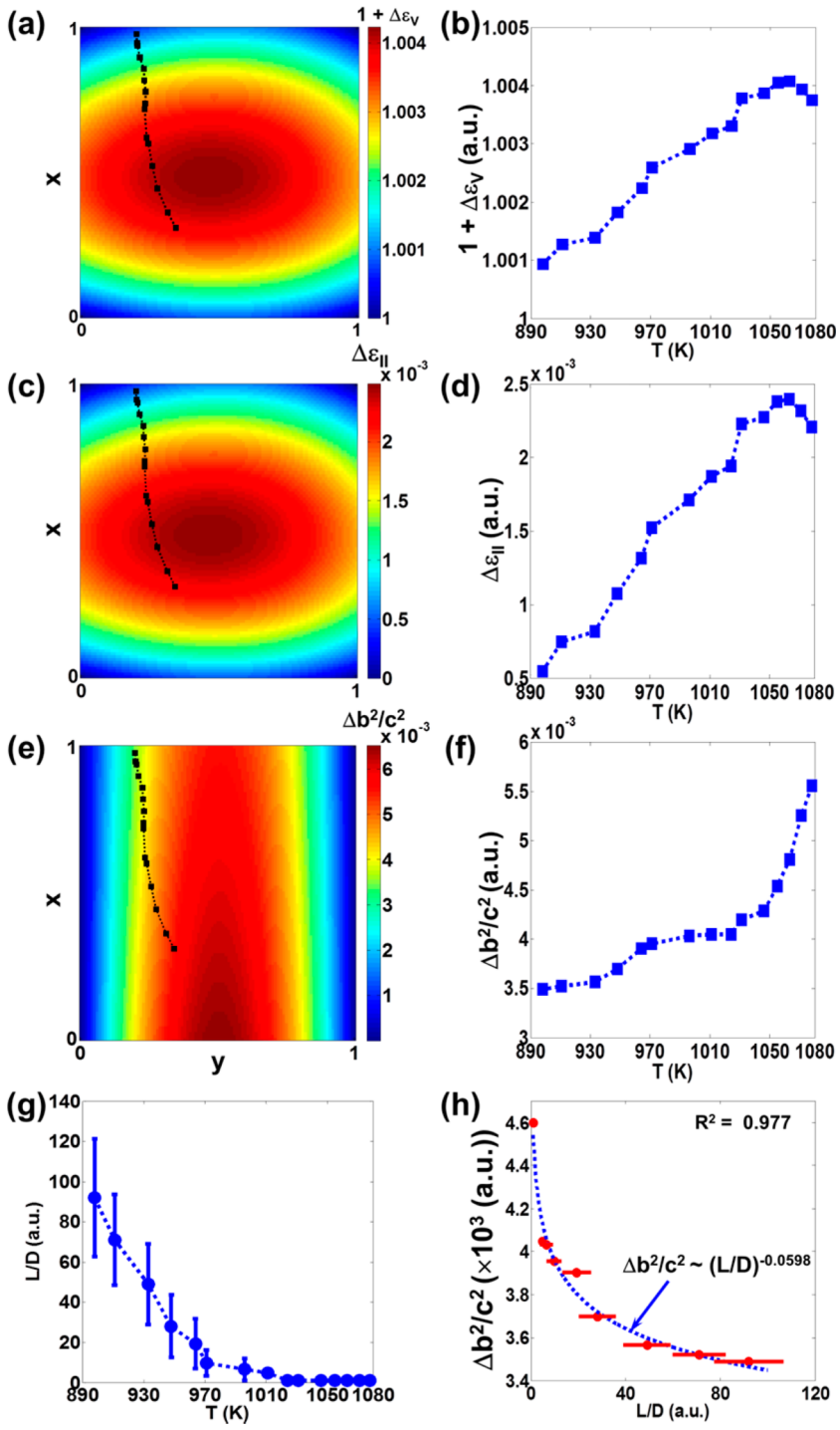

Figure 5. (a) Two-dimensional map for the variations of the volumetric ratio between the concentration-weighted summation of unit cell volumes of HWZ CdS, CdSe, ZnS, and ZnSe and the unit cell volume of HWZ alloy $Cd_xZn_{1-x}S_ySe_{1-y}$ from the VCA model ($1 + \Delta\varepsilon_V$) as a function of *x* and *y*. In the map, black circles are the composition data extracted from the observed alloy nanostructures. (b) Dependence of $1 + \Delta\varepsilon_V$ as a function of *T*. (c) Same as (a) except for the biaxial strain factor $\Delta\varepsilon_{||}$ and (d) dependence of $\Delta\varepsilon_{||}$ as a function of *T*. (e) Same as (a) except for the bond length mismatch parameter ($\Delta b^2/c^2$) and (f) dependence of $\Delta b^2/c^2$ as a function of *T*. (g) Ratio between the width and the thickness of the nanoplate-shaped alloy nanostructures (*L*/*D*) as a function of *T*. (h) Dependence of $\Delta b^2/c^2$ as a function of *L*/*D*. The data are fitted with a power-law function such that $\Delta b^2/c^2 \sim (L/D)^{\alpha}$.

equivalent to the real residual biaxial strain ($\Delta\varepsilon$) because there is neither structural deformation nor a crystalline phase change of the alloy nanostructure. However, it works as a guide to deduce the relative magnitude of the residual strain as a function of the composition of the alloy nanostructures.

In Figure 5a,c, we provided 2D maps for the distribution of $\Delta\varepsilon_V$ (a) and $\Delta\varepsilon_{||}$ (c) as a function of the

composition assuming that $\sigma = 0.3$, which is a typical value for compound semiconductors.[22,23] From the maps, it can be found that the strain factors decrease with decreasing compositional entropy. Given the observed composition at the different growth temperatures, we can analyze the variations of $\Delta\varepsilon_V$ and $\Delta\varepsilon_{||}$, as shown in Figure 5b,d, and from the figure, it is evident that the strain factors decrease from the alloy NWs *via* NBs to NSs. It should be noted that the decreasing behaviors of the strain factors from the NWs to NBs are contrary to the observations of optical bowing (*i.e.*, no bowing for the NWs but the highest bowing for the alloy NBs).

In addition, we can analyze atomic disorder by calculating bond length mismatch which originates from the atomic displacement of the anions from the designated center coordinates of the HWZ unit cell. The bond length mismatch can be the major factor that governs the atomic disorder in the quaternary alloy nanostructures. Indeed, there is a considerable difference of 23.86% in the cationic diameter for Cd^{2+} (1.090 Å) and Zn^{2+} (0.880 Å), and the maximum mismatch can be calculated as 11.84% between CdSe (bond length = 2.630 Å) and ZnS (bond length = 2.335 Å).[22,23] The bond length mismatch for the HWZ unit cell can be calculated as follows:

$$\frac{\Delta b^2}{c^2} \equiv \frac{\langle |{b_c}^2 - {b_{oc}}^2| \rangle}{{c_{VCA}}^2} = 2y(1-y)(x|{b_{C,CdS}}^2 - {b_{C,CdSe}}^2| + (1-x)|{b_{C,ZnS}}^2 - {b_{C,ZnSe}}^2|) \quad (7)$$

where b_c and b_{oc} are for the bond length between the anion and the cation along the *c*-axis and off the *c*-axis, respectively.[25,49,50] A detailed derivation of eq 7 is given in the SI. Using eq 7, we constructed a 2D map (Figure 5e) for the distribution of $\Delta b^2/c^2$ and analyzed variations of $\Delta b^2/c^2$ at different growth temperatures (Figure 5f). As shown in Figure 5f, it is evident that the atomic disorder generated by the bond length mismatch decreases with decreasing growth temperature, as in the context of the strain factors. Thus, it is contrary to the experimental observations of no optical bowing for the alloy NWs and high bowing for the alloy NBs. This implicates the existence of a counterpart that describes the increasing behavior of the degree of bowing reduction from NSs to NWs.

Analysis of the Structural Origin of the Band Gap Bowing Anomaly of the $Cd_xZn_{1-x}S_ySe_{1-y}$ Nanostructures. We translated the behavior between $\Delta b^2/c^2$ and the growth temperature into a relationship between *L*/*D* and $\Delta b^2/c^2$ (Figure 5h) *via* an experimental observation of the dependence of *L*/*D* as a function of the growth temperature (Figure 5g). In Figure 5h, we found that $\Delta b^2/c^2$ can be described by a simple scaling law with respect to *L*/*D* such that $\Delta b^2/c^2 \sim (L/D)^\gamma$ with a scaling exponent as the fitting parameter of $\gamma = -0.0598$ of a satisfactory statistical model correlation coefficient. It is known that the bowing factor can be described as a quadratic function of the short-range order parameter which is strongly dependent on *L*/*D*.[51] Therefore, it is our understanding that the origin of the scaling behavior of $\Delta b^2/c^2$ can be the scaling behavior of the bowing factor with respect to $\Delta b^2/c^2$-dependent short-range order, albeit it appears to not be sufficiently close to the complete scenario for the underlying mechanism that determines the scaling behavior of $\Delta b^2/c^2$ as a function of *L*/*D* with the specific scaling exponent. As shown in Figure 5h, it is clearer that the alloy NWs have the highest atomic disorder while NBs and NSs have smaller disorders. Thus, it is required to reconcile the experimental observation of the structure-dependent optical anomaly concerning the bowing effects and the intrinsic strain factors and atomic disorder behaviors in the nanostructures.

As a semiempirical method, we propose the strain and atomic disorder relaxation factor which is a function of the structure-related variable such as *L*/*D*. In experimental studies on the pseudobinary CdS_xS_{1-x} alloy NWs,[8] we have already observed the disappearance of the optical bowing and shown that the strain relaxation along the *c*-axis and in plane, which is normal to the *c*-axis, is required for the NWs to maintain the single crystallinity without structural and geometrical deformations. This observation is specific for the alloy NWs because the simultaneous relaxations of the uniaxial and biaxial strains are only possible for the elongated structures with a finite diameter that is considerably smaller than the length of the elongated structures.[8] Thus, we can suggest that the strain relaxation factor is equal to zero for the alloy NWs. For the single-crystalline and structurally stable NBs or NSs, it is not required for the alloy nanostructure to relax the biaxial strain over the plane direction if the dimension of the plane is sufficiently larger than the thickness of the structure. Thus, it is expected that the strain relaxation factor would increase with increasing *L*/*D* and saturate for the alloy NSs with a sufficiently large value of *L*/*D*. From these mathematical properties, we can propose a sigmoidal functional form for the strain relaxation factor as a function of *L*/*D*, and one of the simplest forms of the sigmoidal function is a Hill-type function, such that $[(L/D)^\beta - 1]/[(L/D)^\beta - \chi]$, where β and χ are the fitting parameters. When the strain relaxation factor and the scaling behavior of the bond length mismatch are combined, it is possible to construct a semiempirical structural disorder−bowing factor correlation as follows:

$$B \sim (L/D)^\gamma \left[\frac{(L/D)^\beta - 1}{(L/D)^\beta + \chi}\right] \quad (8)$$

where the bowing factor *B* is an entity describing overall bowing which is proportional to the difference

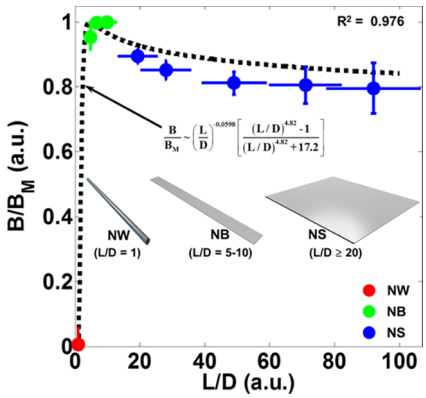

Figure 6. Dependence of the experimentally observed normalized bowing factor (B/B_M) as a function of L/D. Different colored points denote different alloy structures. The data are fitted with the suggested semiempirical equation (black dashed line).

between the expected values of E_g from the VCA model and for experimentally observed values of E_g. In eq 8, it is expected that B is equal to zero for the alloy NWs and rapidly increases as NWs evolve to NBs followed by a slow decrease when the NBs evolve to NSs. This behavior would describe the maximum optical bowing for the NBs. We used the semiempirical correlation in eq 8 to describe the observed bowing factor normalized to the maximum values (*i.e.*, B/B_M) as a function of the morphological parameter, L/D. Based on least-squares fitting, we found that $\beta = 4.82$ and $\chi = 17.2$. As shown in Figure 6, we can find that the semiempirical correlation equation with these fitting parameters effectively describes the observed behaviors of the structure-dependent band gap anomaly of the alloy nanostructures such as the disappearance of the bowing for NWs, maximum bowing for NBs, and smaller yet notable bowing for NSs with a good statistical fitting coefficient. It is also notable that the difference between the NBs and NSs are clearly observable: maximum and nearly constant values for the NBs and smaller and nearly constant values of the NSs.

As shown above, it is evident that there is a structure-dependent optical anomaly, represented by the peculiar optical bowing behaviors of the NWs, NBs, and NSs. It is also possible to distinguish NBs from NSs by examining the structural and optical properties. In terms of band gap modulation engineering, it is important to control and understand how exactly the structure-dependent multicolor light-emitting and light-absorbing properties deviate from the expected band gap, and therefore, it is highly desirable to find a semiempirical yet quantitative correlation on the structure–bowing relationship. Thus, the present experimental study, supported by computational studies with a mathematical model, is beneficial to accurately modulate the band gap of II–VI alloy nanostructures to cover the full visible spectrum.

CONCLUSIONS

In conclusion, we presented experimental, computational, and theoretical studies on the structural and optical properties of single-crystalline HWZ quaternary alloy $Cd_xZn_{1-x}S_ySe_{1-y}$ nanostructures. By changing the growth temperature, composition, molar fractions of components, and morphology, such as nanowires, nanobelts, and nanosheets, of the nanostructures, are varied with maintaining the single crystallinity of the hexagonal wurtzite. From the optical properties measured, we observed an optical bowing disappearance for the alloy NWs and distinct positive optical bowing for NBs and NSs. Using a simple but effective computational method based on the EPM, we found that there is residual strain within the NBs and NS ranging from −1.4 to 1.5%, which results in the optical bowing. From the volumetric strain and bond length mismatch developed in the alloy nanostructures, we found the intrinsic atomic disorder, which was responsible for the bowing factor, decreased as it evolved from NWs *via* NBs to NSs. This decreasing behavior of the bowing origin is balanced with the strain relaxation factor, which increases from NWs at zero to NSs at saturated maximum. By finding a semiempirical correlation between the structure and optical bowing, we explained the observed optical bowing anomaly for the alloy nanostructures. From the analysis, we also found that the different nanostructures can be differentiated from each other by examining residual strain variation inside the structure and optical bowing behavior. The present work is expected to guide band gap engineering by modulating and tailoring the direct band gap of nanostructured semiconductor alloys. In particular, to use a variety of morphologies of the nanostructures, the present work would provide more accurate and effective structure–optical properties correlated to design the desirable band gap to cover specific visible wavelengths for applications in photovoltaic, photocatalytic, and photosensitive materials.

EXPERIMENTAL SECTION

Preparation of the Quaternary Alloy Nanostructures. We grew the quaternary alloy $Cd_xZn_{1-x}S_ySe_{1-y}$ nanostructures *via* the vapor-phase transport of a source vapor onto a substrate by pulsed laser deposition. The source materials for the formation of the alloy nanostructures were prepared by sintering targets in a cylindrical-shaped pellet made of the as-received pure powder mixture of ZnS and CdSe (purity >99.99%, particle size <1 μm, Sigma-Aldrich) with the desired mixing ratio (1:3–3:1 weight ratio) at 700 °C under an Ar–H_2 atmosphere (5 vol % of gaseous H_2). The as-prepared targets were ablated by means of an excimer laser (Lambda Physik, Compex-205, Kr–F radiation, $\lambda = 248$ nm, 25 W, 5 Hz pulse) with an energy density of 3–7 J cm^{-2}. The vapor pressure in the tube of the hot-wall furnace

was uniformly varied in the range of 1 to 10 Torr with 120−150 sccm flow rate. The surface temperature of the prepared target was varied in the range of 1150 to 1300 K. The surface temperature of the substrate was varied by changing the distance from the source and the substrate (d) on which the alloy nanostructures grew (refer to a plot for the measured growth temperature and d in the SI). The temperature inside the quartz tube was measured with thermocouples. The pulsed laser was focused onto the targets, which were placed in the center of the reaction chamber, while the substrate was held in the region in which the temperature was sustained in the range of 890 to 1100 K for a predetermined period of time (1−24 h). For the synthesis of the alloy nanostructures, a thin Au layer, with a typical thickness of 10−20 Å, was deposited onto the cleaned silicon (100) substrate or quartz using ion sputtering. During the growth, the Au thin layer dewets, and the dewetted Au works as a catalyst that drives the VLS process for the formation of the quaternary nanostructures. To examine the morphology of the resulting nanostructures, scanning electron microscopy (Hitachi SE-3000, 20 kV) and field emission scanning electron microscopy (FESEM, Hitachi S-4100, 40 kV) were used. For measurement of the crystallinity, XRD (Bruker D8, Cu Kα radiation, λ = 1.5406 Å) and TEM (JEOL JEM-4010, 200 kV) were used. The composition of each binary compound in the alloy was measured by energy-dispersive X-ray spectroscopy (JEOL JEM-4010, 200 kV) during the TEM examination.

Measurement of the Optical Properties of the Quaternary Alloy Nanostructures. Photoluminescence was excited at room temperature by means of a laser (Spectra Physics Mai Tai VF-T1S Ti: sapphire laser, λ = 400 nm, 0.55 mm WD, 0.60 NA, objective lens of 50×, 1.5 × 10^3 W cm^{-2}) to measure the lowest optical direct band gaps of the as-synthesized alloy nanostructures. The 2 × 2 mm^2 dimension sample was mounted on a pedestal and held at temperatures between 75 and 298 K using a cryostat (JANIS ST-500). The PL signals were collected and detected by a charge-coupled detector (Tokyo Instruments DV 420A-OE). The PL data were measured at 298 K. A scheme for the employed PL system is given in Figure S2 in the SI. For the measurement of the UV−vis Abs signal, we used a microspectrophotometer (μUV−vis, CRAIC 20VM, focal area of 250 × 250 μm^2). For the measurement of the absorbance, the alloy nanostructures grown on the transparent quartz were mounted on the sample holder to which a fiber-optic coupler was focused and detected light from the sample. To extract quantitative information on E_g, the squared intensity of the absorbance was fitted with linear extrapolation, and E_g was matched to the x-intercept of the extrapolation function.

Calculation of the Strain in the Quaternary Alloy Nanostructures. For the analysis of the strain effects for the variation in the band gap of the alloy nanostructures, we employed EPM calculation accompanied by fitting parameters, which accounted for the effects of strains. For the calculations, we used the calibrated atomic factors and potential parameters from the literature.[27−30] The effects of the strain were considered by introducing a fitting parameter set [P_1, P_2] for the local pseudopotential, $V_{loc}(q)$, such that

$$V_{loc}(k) = V_{loc,CdS}(k)xy + V_{loc,CdSe}(k)x(1-y) + V_{loc,ZnS}(k)(1-x)y + V_{loc,ZnSe}(k)(1-x)(1-y) - P_1x^2y - P_2y^2x \quad (9)$$

where k is the reciprocal wavenumber, and it is found from fitting with the experimental data that [P_1, P_2] = [−0.225, 0.092] for the tensile strain and [P_1, P_2] = [−0.305, 0.114] for the compressive biaxial strain. We used the VCA model for the nonlocal pseudopotential and ionic parameters including elastic constants. Given the calibrated parameters, we examined the band gap variation of the alloy nanostructures with a given composition to find the effective residual strains in the alloy nanowires, as shown in Figure 4a,b. Using an arbitrary combination of the compositions x and y, we also calculated E_g, from which we calculated the bowing equation parameters for the nanostructures used in Figure 4d,e with residual tensile and compressive strain, respectively. Detailed information on the EPM is given in the SI.

Conflict of Interest: The authors declare no competing financial interest.

Acknowledgment. This research was financially supported by the KIST institutional research program (2E25373) and the Pioneer Research Center Program through the National Research Foundation of Korea funded by the Ministry of Science, ICT & Future Planning (NRF-2013M3C1A3065033). S.J.K., H.M.J., G.T.K., and J.G.P. designed the experiments. S.J.K. and H.M.J. measured and analyzed the structural data. S.J.K., H.M.J., D.H.K., H.D.K., I.K.H., and J.G.P. measured and analyzed the optical data. S.J.K. calculated electronic band structure and strain effects. K.N.J. helped to prepare Figure 6. S.J.K. constructed a theoretical model to extract bowing−structure correlation. S.J.K., H.M.J., and J.G.P. wrote the draft.

Supporting Information Available: Schematic illustration for the PLD system, temperature variation inside the quartz tube as a function of the distance between the target source and the substrate, a dark-field TEM image of Au tip−NW interface, a schematic illustration for the PL measurement system, the detailed information on the EPM calculation method, a schematic illustration of HWZ unit cell of the alloy nanostructures, configurations of tetrahedral bonds in the alloy HWZ unit cells, and proof of eq 7 are given. This material is available free of charge *via* the Internet at http://pubs.acs.org.

REFERENCES AND NOTES

1. Peng, X.; Schlamp, M. C.; Kadavanich, A. V.; Alivisatos, A. P. Epitaxial Growth of Highly Luminescent CdSe/CdS Core/Shell Nanocrystals with Photostability and Electronic Accessibility. *J. Am. Chem. Soc.* **1997**, *119*, 7019–7020.
2. Wada, Y.; Yin, H.; Kitamura, T.; Yanagida, S. Photoreductive Dechlorination of Chlorinated Benzene Derivatives Catalyzed by ZnS Nanocrystallites. *Chem. Commum.* **1998**, 2683–2684.
3. Duan, X. F.; Lieber, C. M. General Synthesis of Compound Semiconductor Nanowires. *Adv. Mater.* **2000**, *12*, 298–302.
4. Duan, X. F.; Huang, Y.; Agarwal, R.; Lieber, C. M. Single-Nanowire Electrically Driven Laser. *Nature* **2003**, *421*, 241–245.
5. Sheeny-Haj-Ichia, L.; Wasserman, J.; Willner, I. CdS-Nanoparticle Architectures on Electrodes for Enhanced Photocurrent Generation. *Adv. Mater.* **2002**, *14*, 1323–1326.
6. Huang, Y.; Duan, X. F.; Lieber, C. M. Semiconductor Nanowire for Multi-color Photonics. *Small* **2005**, *1*, 142–147.
7. Kyukendall, T.; Ulrich, P.; Aloni, S.; Yang, P. Complete Composition Tunability of InGaN Nanowires Using a Combinatorial Approach. *Nat. Mater.* **2007**, *6*, 951–956.
8. Kwon, S. J.; Choi, Y. J.; Park, J. H.; Hwang, I. S.; Park, J. G. Structural and Optical Properties of CdS_xSe_{1-x} Nanowires. *Phys. Rev. B* **2005**, *72*, 205312/1–205312/7.
9. Liu, Y.; Zaplen, J. A.; Shan, Y. Y.; Geng, C. Y.; Lee, C. S.; Lee, S. T. Wavelength Controlled Lasing in $Zn_xCd_{1-x}S$ Single Crystal Nanoribbons. *Adv. Mater.* **2005**, *17*, 1372–1377.
10. Venugopal, R.; Lin, P.; Chen, Y. T. Photoluminescence and Raman Scattering from Catalytically Grown $Zn_xCd_{1-x}Se$ Alloy Nanowires. *J. Phys. Chem. B* **2006**, *110*, 11691–11696.
11. Pan, A.; Wang, X.; He, P.; Zhang, Q.; Wan, Q.; Zacharias, M.; Zhu, X.; Zou, B. Color-Changeable Optical Transport through Se-Doped CdS 1D Nanostructures. *Nano Lett.* **2007**, *7*, 2970–2975.
12. Pan, A.; Zhou, W.; Leong, E. S. P.; Liu, R.; Chin, A. H.; Zou, B.; Ning, C. Continuous Alloy-Composition Spatial Grading and Superbroad Alloy-Composition Spatial Grading and Superbroad Wavelength-Tunable Nanowire Lasers on a Single Chip. *Nano Lett.* **2009**, *9*, 784–788.
13. Deng, Z.; Yan, H.; Liu, Y. Band Gap Engineering of Quaternary-Alloyed ZnCdSSe Quantum Dots *via* a Facile Phosphine-Free Colloidal Method. *J. Am. Chem. Soc.* **2009**, *131*, 17744–17745.
14. Bhattacharyya, S.; Estrin, Y.; Moshe, O.; Rich, D. H.; Solovyov, L. A.; Gedanken, A. Highly Luminescent $Zn_xCd_{1-x}Se$/C Core/Shell Nanocrystals: Large Scale Synthesis, Structural and Cathodoluminescence Studies. *ACS Nano* **2009**, *3*, 1864–1876.

15. Hewa-Kasakarage, N. N.; El-Khoury, P. Z.; Tarnovsky, A. N.; Kirsanova, M.; Nemitz, I.; Nemchinov, A.; Zamkov, M. Ultrafast Carrier Dynamics in Type II ZnSe/CdS/ZnSe Nanobarbells. *ACS Nano* **2010**, *4*, 1837–1844.
16. Pan, A.; Liu, R.; Sun, M.; Ning, C. Quaternary Alloy Semiconductor Nanobelts with Bandgap Spanning the Entire Visible Spectrum. *J. Am. Chem. Soc.* **2009**, *131*, 9502–9503.
17. Pan, A.; Liu, R.; Sun, M.; Ning, C. Spatial Composition Grading of Quaternary ZnCdSSe Alloy Nanowires with Tunable Light Emission between 350 and 710 nm on a Single Substrate. *ACS Nano* **2010**, *4*, 671–680.
18. Yasuda, H.; Mori, H. Spontaneous Alloying in Atom Clusters in the ZnS−CdSe Pseudo-binary System. *Intermetallics* **1996**, *4*, S225–S228.
19. Korostelin, Yu. V.; Kozlovsky, V. I.; Nasibov, A. S.; Shapkin, P. V. Vapour Growth of II−VI Solid Solution Single Crystals. *J. Cryst. Growth* **1996**, *159*, 181–185.
20. Zunger, A.; Jaffe, J. E. Structural Origin of Optical Bowing in Semiconductor Alloys. *Phys. Rev. Lett.* **1983**, *51*, 662–665.
21. Behringer, M.; Ohkawa, K.; Grobmann, V.; Heinke, H.; Leonardi, K.; Fehrer, M.; Hommel, D.; Kuttler, M.; Strassburg, M.; Bimber, D. Stability Issues of Quaternary CdZnSSe and Ternary CdZnSe Quantum Wells in Blue-Green Laser Diodes. *J. Cryst. Growth* **1998**, *184/185*, 580–584.
22. Tamargo, M. C. *II−VI Semiconductor Materials and Their Applications*; Taylor & Francis: New York, 2002.
23. Hernandez-Calderan, I. *Optical Properties & Electronic Structure of Wide Band Gap II−VI Semiconductors in II—VI Semiconductor Materials & Their Applications*; Taylor & Francis: New York, 2002; pp 113−170.
24. Van Vechten, J. A.; Bergstresser, T. K. Electronic Structures of Semiconductor Alloys. *Phys. Rev. B* **1970**, *1*, 3351–3358.
25. Zunger, A.; Jaffe, J. E. Structural Origin of Optical Bowing in Semiconductor Alloys. *Phys. Rev. Lett.* **1983**, *51*, 662–665.
26. Harrison, W. A. *Electronic Structure and the Properties of Solids: The Physics of the Chemical Bond*; Freeman: San Francisco, 1980.
27. Cohen, M. L.; Bergstresser, T. K. Band Structures and Pseudopotential Form Factors for Fourteen Semiconductors of the Diamond and Zinc-Blende Structures. *Phys. Rev.* **1966**, *141*, 789–796. Bergstresser, T. K.; Cohen, M. L. *Phys. Rev.* **1967**, *164*, 1069–1080.
28. Chelikowsky, J. R.; Cohen, M. L. Nonlocal Pseudopotential Calculations for the Electronic Structure of Eleven Diamond and Zinc-Blende Semiconductors. *Phys. Rev. B* **1976**, *14*, 556–582.
29. Zakharov, O.; Rubio, A.; Blasé, X.; Cohen, M. L.; Louie, S. G. Quasiparticle Band Structures of Six II−VI Compounds: ZnS, ZnSe, ZnTe, CdS, CdSe, and CdTe. *Phys. Rev. B* **1994**, *50*, 10780–10787.
30. Feng, Y. P.; Teo, K. L.; Lim, F.; Poon, H. C.; Ong, C. K.; Xia, J. B. Empirical Pseudopotential Band-Structure Calculation for $Zn_xCd_{1-x}S_ySe_{1-y}$ Quaternary Alloy. *J. Appl. Phys.* **1993**, *74*, 3948–3955.
31. Long, F.; Harrison, P.; Hagston, W. E. Empirical Pseudopotential Calculations of $Cd_{1-x}Mn_xTe$. *J. Appl. Phys.* **1996**, *79*, 6939–6942.
32. Rezaei, B.; Asgari, A.; Kalafi, M. Electronic Band Structure Pseudopotential Calculation of Wurtzite III-Nitride Materials. *Phys. B* **2006**, *371*, 107–111.
33. Gershoni, D.; Temkin, H.; Vandenberg, J. M.; Chu, S. N. G.; Hamm, R. A.; Panish, M. B. Type-I to Type-II Superlattice Transition in Strained Layers of $In_xGa_{1-x}As$ Grown on InP. *Phys. Rev. Lett.* **1988**, *60*, 448–451.
34. Kim, J.; Fischetti, M. V. Electronic Band Structure Calculations for Biaxially Strained Si, Ge, and III−V Semiconductors. *J. Appl. Phys.* **2010**, *108*, 013710.
35. Kim, J.; Fischetti, M. V.; Aboud, S. Structural, Electronic, and Transport Properties of Silicane Nanoribbons. *Phys. Rev. B* **2012**, *86*, 205323.
36. Li, X. L.; Wang, C. X.; Yang, G. W. Thermodynamic Theory of Growth of Nanostructures. *Prog. Mater. Sci.* **2014**, *64*, 121–199.
37. Yang, Y.; Ryi, S.; Cai, W. A Three-Dimensional Phase Field Model for Nanowire Growth by the Vapor−Liquid−Solid Mechanism. *Modell. Simul. Mater. Sci. Eng.* **2014**, *22*, 055005.
38. Kwon, S. J. Theoretical Analysis of Non-catalytic Growth of Nanorods on a Substrate. *J. Phys. Chem. B* **2006**, *110*, 3876–3882.
39. Kwon, S. J. Theoretical Analysis of the Radius of Semiconductor Nanowires Grown by the Catalytic Vapour−Liquid−Solid Mechanism. *J. Phys.: Condens. Matter* **2006**, *18*, 3875–3886.
40. Vegard, L. Die Konstitution der Mischkristalle und die Raumfullung der Atome. *Z. Phys.* **1921**, *5*, 17–26.
41. Kwok, H. S.; Zheng, J. P.; Witanachchi, S.; Shi, L.; Shaw, D. T. Growth of CdS_xSe_{1-x} Thin Films by Laser Evaporation Deposition. *Appl. Phys. Lett.* **1988**, *52*, 1815–1816.
42. Vijayalakshmi, R. P.; Venugopal, R.; Reddy, D. R.; Reddy, B. K. Structural and Bandgap Studies of ZnSCdSe Thin Films. *Semicond. Sci. Technol.* **1994**, *9*, 1062–1068.
43. Wei, S. H.; Zunger, A. Band Offsets and Optical Bowings of Chalcopyrites and Zn-Based II−VI Alloys. *J. Appl. Phys.* **1995**, *78*, 3846–3856.
44. Chen, A.-B.; Sher, A. Gap Variation in Semiconductor Alloys and the Coherent-Potential Approximation. *Phys. Rev. Lett.* **1978**, *40*, 900–903.
45. Hohenberg, P.; Kohn, W. Inhomogeneous Electron Gas. *Phys. Rev.* **1967**, *136*, B864–B871.
46. Wei, S. H.; Ferreira, L. G.; Bergnard, J. E.; Zunger, A. Electronics Properties of Random Alloys: Special Quasirandom Structures. *Phys. Rev. B* **1990**, *42*, 9622–9649.
47. Mader, K. A.; Zunger, A. Short- and Long-Range-Order Effects on the Electronic Properties of III−V Semiconductor Alloys. *Phys. Rev. B* **1995**, *51*, 10462–10476.
48. Fermi, E. Sopra lo Spostamento per Pressione delle Righe Elevate delle Serie Spettrali. *Nuovo Cimento* **1934**, *11*, 157–166.
49. Jaffe, J. E.; Zunger, A. Anion Displacements and the Band-Gap Anomaly in Ternary ABC_2 Chalcopyrite Semiconductors. *Phys. Rev. B* **1983**, *27*, 5176–5179.
50. Jaffe, J. E.; Zunger, A. Theory of the Band-Gap Anomaly in ABC_2 Chalcopyrite Semiconductors. *Phys. Rev. B* **1984**, *29*, 1882–1906.
51. Mascarenhas, A. *Spontaneous Ordering in Semiconductor Alloys*; Kluwer Academic Publishers: New York, 2002.